REGULAR PAPER

Two-step pulse compressor based on asymmetric four-grating compressor for femtosecond petawatt lasers

Xiong Shen[1,3] · Shuman Du[1,2] · Wenhai Liang[1,2] · Peng Wang[1,3] · Jun Liu[1,2,3] · Ruxin Li[1,2,3]

Abstract

Laser-induced damage of compression gratings has become the shortest stave for petawatt (PW) laser facilities, as it is hard to manufacture large enough meter-sized gratings with high damage threshold. Multistep pulse compressor (MPC) was proposed to improve the peak power of PW lasers recently. Using the asymmetric four-grating compressor (AFGC) to replace both of the prism-pair-based pre-compressor and typical four-grating compressor (FGC)-based main compressor, the typical three-step MPC is simplified to two steps, and can be easily extended to all PW lasers by simply reducing and increasing same amount of suitable distances of the two grating pairs, respectively. Furthermore, the AFGC will induce spatial dispersion and direct smooth the laser beam on the last grating, which is the easiest to be damaged one, and then protect it away from damage and increase the operating safety straightly. More than 100 PW can be achieved without beam combination theoretically using the AFGC-based two-step MPC method with currently available biggest gold-coated gratings.

1 Introduction

Petawatt (PW) lasers benefited from advanced optical techniques, especially the chirped pulse amplification (CPA) [1] and the optical parametric CPA (OPCPA) [2], are emerging across the world, and more than 50 facilities are either operational, under construction or in the planning phase [3]. Among them, both the SULF facility in China (SULF-10 PW) and the ELI-Nuclear Physics (ELI-NP) in Romania have already achieved the currently highest peak power of 10 PW recently [4, 5].

Researches in the relativistic optical research field have been promoted by these PW class lasers with focal intensities higher than 10^{18} W/cm^2 [6]. The extremely high optical-field conditions provide powerful tools for many ultrahigh-field researches, such as particle acceleration, high energy secondary sources generation, laboratory astrophysics and nonlinear QED. Scientists are even imagining the use of a future 100 PW laser (SEL-100 PW), that has been started in 2018 [7], in the frontier scientific research of vacuum birefringence with extremely high 10^{23-24} W/cm^2 focal intensity [8]. These attractive applications have become the main motivation on the development of PW lasers in turn.

The principle of achieving femtosecond PW lasers can be summed up in three steps: Firstly, the seed pulse is stretched from femtosecond to nanosecond; Secondly, the stretched pulse is amplified to hundreds or even thousands of Joules in gain media by using the CPA or the OPCPA techniques; Finally, the amplified nanosecond stretched pulse is compressed back to femtosecond pulse by using grating-based pulse compressor. Laser-induced damage of gratings in the final pulse-compression-step is the shortest stave for PW facilities, as it is hard to manufacture large enough meter-sized gratings with high damage threshold, especially for 10 s to 100 s of PWs lasers [9, 10].

Tiled grating (or mosaic grating) is a direct grating enlarging method to overcome the maximum compressed pulse energy output limitation. In the method, a large-sized

---

Xiong Shen and Shuman Du contributed equally to this work.

✉ Xiong Shen
xshen@siom.ac.cn

✉ Jun Liu
jliu@siom.ac.cn

1 State Key Laboratory of High Field Laser Physics and CAS Center for Excellence in Ultra-Intense Laser Science, Shanghai Institute of Optics and Fine Mechanics, Chinese Academy of Sciences, Shanghai 201800, China

2 University Center of Materials Science and Optoelectronics Engineering, University of Chinese Academy of Sciences, Beijing 100049, China

3 Zhangjiang Laboratory, 100 Haike Road, Pudong, Shanghai 201210, China

grating is composed of several small-sized gratings [11]. It is easy to manufacture small-sized gratings, while each of the composed small-sized grating components must be tiled precisely with six degrees of freedom: piston and shift, groove spacing and tilt, and rotation and tip [9], which results in new control challenges. What is more, gaps between adjacent tile gratings can affect the integrality of spectrum and result in diffraction-induced intensity modulation, which may affect the spatiotemporal property of the output laser and damage the followed optical components.

Coherent beam combination (CBC) is another method to increase the maximum compressed pulse energy output that has been extensively studied and applied for PW lasers [12]. Laser beams are split into N sub-beams prior to amplifier [13], compressor [14, 15], or even in the compressor [9], and followed by recombining of the compressed N sub-beams. However, the CBC method is complicated as it is sensitive to the differences of optical delay, pointing stability, wavefront, and dispersion among the N sub-beams [9, 16].

Spatial intensity profile of the amplified laser beam is another important factor that affects the maximum compressed output pulse energy except for the limitation laser-induced damage of gratings. Since the laser spatial intensity modulations (LSIM), generally defined as the ratio between the maximum local intensity to the average beam intensity, of beams output from the final amplifiers in PW facilities are relatively high, generally as high as approximately 2.0. Then, the average fluence on compression gratings is usually set to be approximately half of the laser-induced damage threshold of compression gratings for the operating safety [17].

Multistep pulse compressor (MPC) was proposed recently to reduce the LSIM in the compressor and increase the whole compressed pulse energy output [17]. Typically, in MPC, there are three steps: a prism pair used for the pre-compressor to introduce a certain amount of spatial dispersion; a typical four-grating compressor (FGC) with symmetric configuration used for the main compressor; and a spatiotemporal focusing-based self-compressor used for the post-compressor. The spatial dispersion introduced by the prism pair smooths the laser beam, which increases the bearable output pulse energy of the compressor.

In this study, we further simplify the typical three-step MPC using an asymmetric optical design of the FGC. An asymmetric four-grating compressor (AFGC) is used to replace both the prism-based pre-compressor and the symmetric FGC based main compressor simultaneously. The influences of the AFGC configuration to the spatiotemporal properties of the output laser are analyzed in detail. The introduced spatial dispersion smooths the laser beam on the final grating of the compressor and improve the maximum bearable output pulse energy and operating safety of the compressor. By introducing a spatial dispersion width of 60 mm by the AFGC, the LSIM of the output beam can be decreased from approximately 2.0–1.1 theoretically. It means that more than 1.5 times increasing of the output pulse energy from the AFGC is possible in comparison to a traditional FGC with symmetric configuration in theory [18]. As a result, more than 100 PW laser can be achieved theoretically with single laser beam incident to the AFGC, composed of four currently available biggest gratings. In comparison to typical three-step MPC, this AFGC-based two-step MPC can be easily extended to all exist PW laser facilities because it needs neither additional optical component nor additional optical controlling.

2 Two important factors in a compressor

Gold-coated gratings are the main choice for femtosecond PW laser compressors. This is because gold-coated gratings own high diffraction efficiencies over broadband spectra which can support ultrashort pulse output [19]. There are two important factors that should be taken into consideration in a gold-coated grating based compressor.

Pulse duration is one of them. Experimental data have been concluded that the laser-induced damage threshold fluence of nanosecond pulses is approximately 2–3 times higher than that of femtosecond pulses [10, 17]. Then, in an FGC, although the first grating bears the highest pulse energy, the final grating stands the biggest risk of laser-induced damage due to the shortest pulse duration. Considering approximately 90% diffraction efficiency of each gold-coated grating, the first grating can bear about twice pulse energy than that of the final grating. This property has been used in the in-house beam-splitting pulse compressor method recently [9] to simplify the CBC-based PW pulse compressors.

LSIM is the other one. The LSIM of the laser beam incident to the compressor is generally as high as approximately 2.0. To avoid laser-induced damage of the gratings, the fluence on the final grating is usually designed to be under half of its laser-induced damage threshold when considering the LSIM of laser beam. Then, reducing the LSIM on the compressor gratings, especially the final grating, is also an effective method to increase the maximum peak power of PW lasers [17].

3 AFGC based two-step MPC

3.1 Structure of an AFGC

The optical configuration of an AFGC is demonstrated in Fig. 1. $L1$ is the distance between $G1$ and $G2$, and $L2$ is the distance between $G3$ and $G4$. $L1 \neq L2$ makes it different from a typical FGC with symmetric configuration that $L1 = L2$.
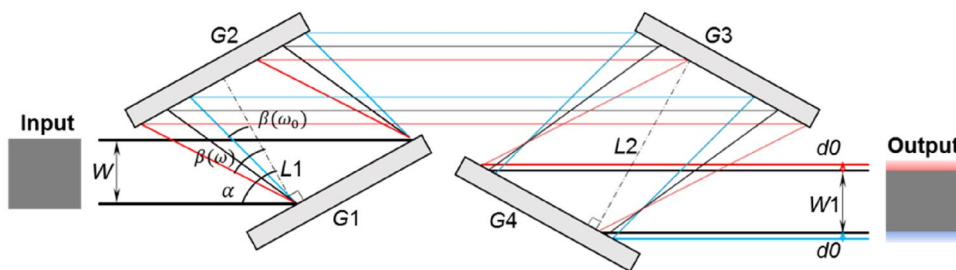
Fig. 1 Optical configuration of an AFGC. W, W1, widths with full spectral components along the horizontal direction in the input and output beams, respectively. G1-4, diffraction gratings. L1, L2, per- pendicular distances of the first and second grating pair, respectively. d0, induced spatial dispersion width with partial spectral components along the horizontal direction in the output beam

Here, $L1$ is shorter than $L2$, which makes the output laser beam wider than that of the input beam with no spatial dispersion.

For an AFGC, similar to a single prism pair or grating pair, the asymmetric structure will induce obvious spatial disper- sion to the output beam from the compressor. What is more, according to the principle of Treacy compressor, the induced spectral dispersion is proportional to the grating distance for the same gratings and same incident angle, which makes AFGC possible to introduce absolutely the same amount of spectral dispersion to compress the chirped pulses in compari- son to that of a typical FGC with symmetric configuration if only $L1 + L2$ is equal for both optical designs. These two fea- tures of AFGC makes it can be used as both the prism-based pre-compressor to induce spatial dispersion, and the typical FGC-based main compressor to induce main spectral disper- sion simultaneously in an MPC.

Furthermore, owing to the relative strong diffraction ability of gratings, large width of spatial dispersion can be obtained with a small different distance between $L1$ and $L2$. As a result, the output laser beam after an AFGC is well smoothed owing to the introduced spatial dispersion. Moreover, since the last grating $G4$ the one that stands the biggest risk of laser-induced damage, the spatial dispersion can protect it straightly from laser induced damage mainly due to far-field hot spots. Note that this AFGC configuration was also proposed in a picosec- ond PW laser system to smooth the tiled-grating gap induced output intensity modulation about a decade ago, where only approximately 2-mm spatial dispersion was introduced to the output laser beam of the OMEGA-EP facility due to the nar- row spectral bandwidth [20].

The amount of spatial dispersion width d of two frequency components ω and ω_0 introduced by a grating pair with per- pendicular distance of L is shown in Fig. 2, which can be described as:

$$d = \left(\tan \beta\left(\omega_0\right) - \tan \beta\left(\omega\right)\right) \cos \alpha * L \tag{1}$$
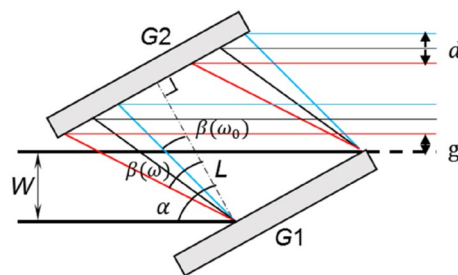

Fig. 2 Spatial dispersion introduction by a grating pair. G1-2, diffrac- tion gratings. W, width of the input beam along the horizontal direc- tion. α, incident angle. $\beta(\omega)$ and $\beta(\omega_0)$, diffraction angles of the fre- quencies ω and ω_0, respectively. L, perpendicular length between G1 and G2. d, induced spatial dispersion width of the output beam. g, gap width between G1 up edge and the output beam down edge from G2

The gap between the up edge of $G1$ and lower edge of the beam exiting $G2$ is:

$$g = L / \cos \left(\beta(\omega)\right) * \sin \left(\alpha - \beta(\omega)\right) - W \tag{2}$$

Then, the induced spatial dispersion $d0$ on one side of an AFGC, which is shown in Fig. 1, can be expressed as:

$$d0 = \left(\tan \beta\left(\omega_s\right) - \tan \beta\left(\omega_l\right)\right) \cos \alpha * (L2 - L1) \tag{3}$$

where ω_s and ω_l represent the shortest and the longest wave- length of the input laser beam, α is the incident angle on the grating. For a general symmetric FGC with $L1 = L2$, there is no spatial dispersion with $d0 = 0$, while for an AFGC, $d0 \neq 0$. From Eq. (3), the induced spatial dispersion width $d0$ is linearly related to the difference between the two per- pendicular distances $L1$ and $L2$. However, to keep $L1 + L2$ a constant, the increasing of $L2$ will accompanied by the decreasing of $L1$, which means the first grating may induce light obstructing for a small $L1$ that should be carefully con- sidered simultaneously.

3.2 Beam smoothing by an AFGC

The OPCPA technique has been a preferable solution of pulse amplification for 10–100 s PW level laser facilities [3]. This is because the nonlinear crystals for amplification, LBO or DKDP mainly, can support ultrashort pulse output with spectral bandwidth wider than 200 nm centered at about 925 nm. What is more, the aperture of DKDP can even be larger than 40 cm that is enough for high pulse energy output.

In the OPCPA stage of PW facilities, limited by the factors such as pump laser beam quality, heat control and homogeneity of large scale optics and nonlinear crystals, the output amplified laser beam owns high beam spatial intensity modulation with LSIM larger than 2.0 according to experimental measurement.

The beam wavefront always contains distortions caused by imperfect optical components and diffraction of edges and dusts. It can be classed into three parts with high, middle and low spatial frequencies, and the low spatial frequency part can be compensated by using deformable mirrors. Similarly, the modulation of the beam spatial intensity distribution can also be classed into three parts with high, middle and low spatial frequencies, and the low spatial frequency part is usually relative small in comparison to the other two parts. Therefore, only the high and middle spatial frequency parts of both the intensity modulation and wavefront distortion should be considered.

In PW facilities, spatial filtering is used to remove wavefront distortion at high spatial frequency which will induce intensity modulation during propagation. While, for the final grating in the compressor that stands the biggest risk of laser-induced damage, the intensity modulation on it is decided by the middle and low spatial-frequency of wavefront distortion and modulations of intensity distribution. The wavefront distortion of imperfect large optical components after the final spatial filter, such as the beam collimating parabolic reflective mirror, the plane reflective mirror or even the rest three gratings in the compressor can induce high spatial intensity modulation. There is no smoothing mechanism to solve these modulations in PW facilities based on a typical FGC, even in the MPC method proposed recently, and should be taken into consideration carefully. While, the AFGC in this study can introduce moderate spatial dispersion to the beam and smooth the intensity modulation effectively on the final grating to protect it, which will increase the maximum compressed pulse energy output from the compressor.

To verify the beam smoothing capacity of the AFGC, single Gaussian-shape hot spots with different FWHM diameters (0.25, 0.5, 1, 2, 4, 6, 8 (mm)) are added to simulated laser beam. The beam profile is assumed to be square 10th order super-Gaussian profile with 500×500 mm² full area,

and the chirped pulse duration is set to be 4 ns and centered at 925 nm with a full spectral bandwidth of approximately 200 nm and a 6th order super-Gaussian profile. The grating groove density used is set to be 1400 lines/mm and the incident angle of the compressor 61°. The total perpendicular length of the two grating pairs, $L1 + L2$, is approximately 2480 mm to compensate the chirped pulse to a Fourier-transform limited (FTL) pulse of duration approximately 14.7 fs according to the principle of Treacy compressor [18].

Figure 3a shows the 500 mm full width ideal 10th order super-Gaussian beam profile with a hot spot of Gaussian shape, Fig. 3b and c are the spectrum profile and its FTL temporal profile, respectively. The hot spot is distributed in the middle of the beam, and leads the LSIM of the beam to be approximately 2.0. With the increase of the introduced spatial dispersion width, the LSIMs that induced by hot spot of Gaussian shape with different FWHM diameters [0.25, 0.5, 1, 2, 4, 6, 8 (mm)] decrease as shown in Fig. 3d (Left Y axis). The LSIMs decrease rapidly at first and then slowly as the spatial dispersion width keep increasing.

Just 5-mm spatial dispersion width is enough to smooth the LSIM from 2.0 to 1.3 for beams own hot spots with FWHM diameters smaller than 1 mm, and even to 1.1 for beams own hot spots with FWHM diameters smaller than 0.5 mm. Approximately 30-mm and 60-mm spatial dispersion width can smooth LSIMs from 2.0 to 1.1 for beams own hot spots with FWHM diameters smaller than 2 mm and 4 mm, respectively. From the simulation shown in Fig. 3d, we can conclude that a small amount of spatial dispersion even less than 10 mm can do a big favor to smooth the beam and increase the maximum bearable output pulse energy and operating safety of the compressor.

Figure 3d also shows the introduced spatial dispersion width variation to the change of $L2$-$L1$ of an AFGC with 1400 lines/mm grating groove density and 61° incident angle. As a comparison, the introduced spatial dispersion width variation to the distance of a fused silica prism pair with 30° apex angle and 0° incident angle is also shown. Obviously, to introduce a suitable spatial dispersion width for effective LSIM decrease, tens of meters distance is required for a prism pair, while just tens of centimeters distance between $L2$-$L1$ is required for an AFGC.

We add seven hot spots on a beam simultaneously with equal interval distributed in the middle along the vertical direction as shown in Fig. 4a to explain the influence of spatial frequency in the intensity modulation directly. Three hot spots with diameters less than 2 mm can hardly be observed as the 500×500 mm² beam profile dimension is too large.

Spatial dispersion widths of $d0 = 10$ mm and $d0 = 60$ mm along the horizontal direction (perpendicular to the grating groove lines) are used for the simulation. According to grating equation and Eq. (3), the distance difference between $L2$ and $L1$, that is $L2$-$L1$, should

Fig. 3 **a** Beam profile with a hot spot of Gaussian shape distributed in the middle. **b** Spectrum profile, and its FTL temporal profile **c**. **d** LSIM variations to introduced spatial dispersion width (left Y axis) for beams with different FWHM diameters (0.25, 0.5, 1, 2, 4, 6, 8 (mm)); prism pair distance, and distance difference between $L2$ and $L1$ of an AFGC that needed for different spatial dispersion width (right double Y axes)
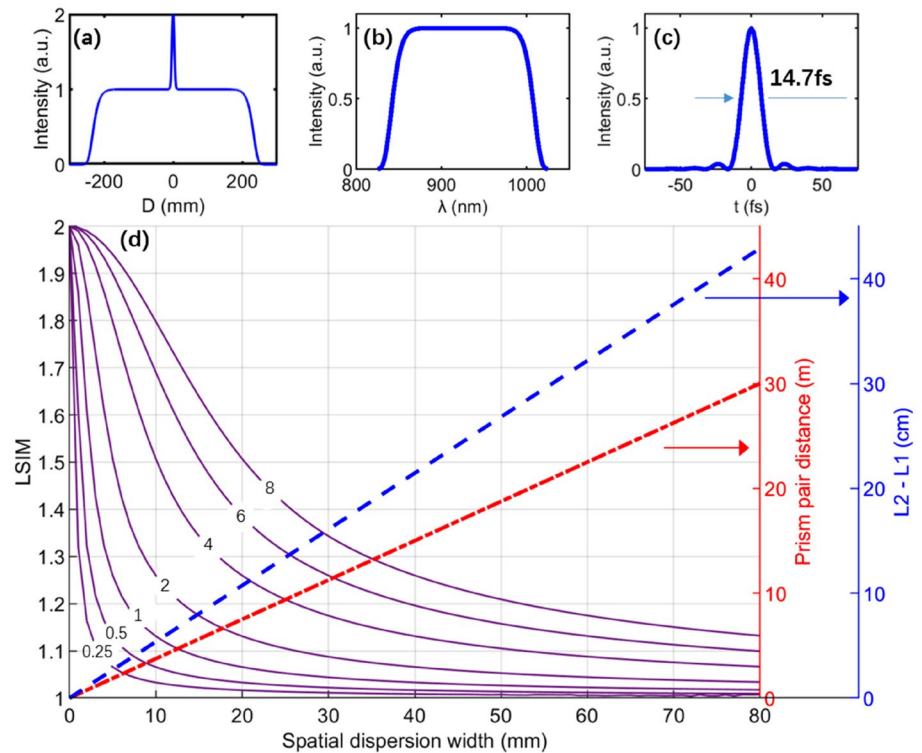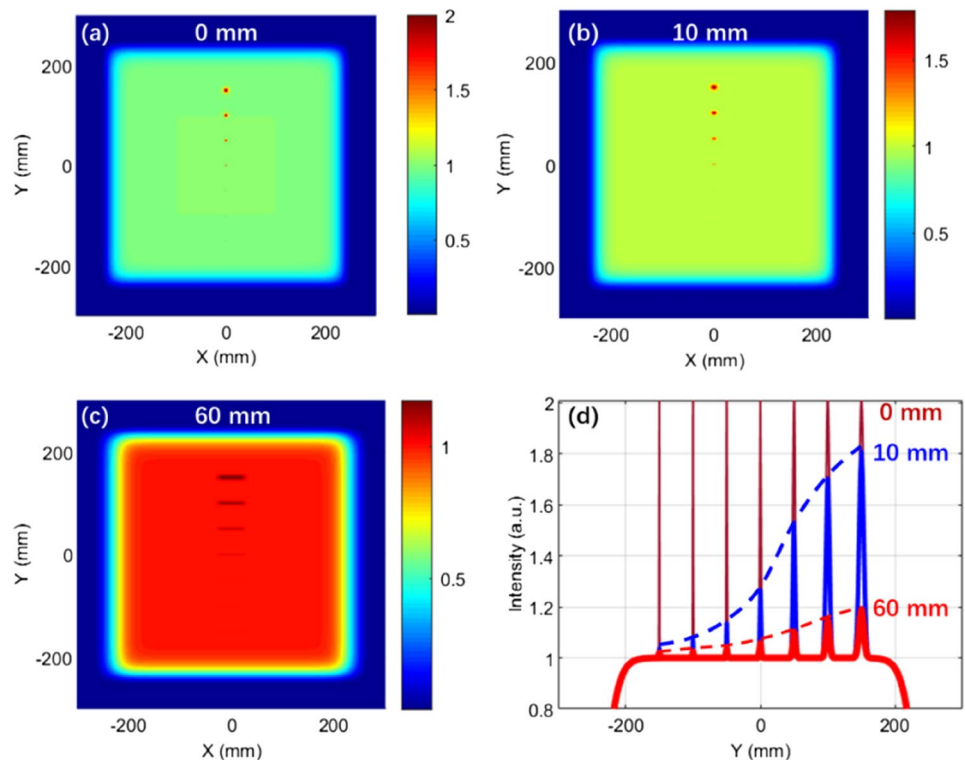

Fig. 4 **a** Input beam profile with seven Gaussian shape hot spots and different FWHM diameters (0.25, 0.5, 1, 2, 4, 6, 8 (mm)) simultaneously along the vertical direction. **b** and **c** Output beam profiles from the AFGC with the induced spatial dispersion $d0$ are approximately 10 mm and 60 mm, respectively. **d** Beam profiles at $X=0$ of the input and two output beams

be approximately 54 mm and 322 mm for $d0 = 10$ mm and $d0 = 60$ mm, respectively. Then, the distances $L1$ between $G1$ and $G2$ are set to be 1213 mm/1079 mm, and the distances $L2$ between $G3$ and $G4$ are set to be 1267 mm/1401 mm as for $d0$ is 10 mm/60 mm, respectively. With the beam profile shown in Fig. 4a used as the

input beam, Fig. 4b and c show the output beam profiles from the AFGC with the induced spatial dispersion $d0$ are approximately 10 mm and 60 mm, respectively. Hot spots are stretched along the diffraction direction in accordance with the spatial dispersion introduced, which smooths the beam.

Figure 4d shows the beam profiles at $X = 0$ of the input and two output beams. We can see that 10-mm spatial dispersion width can effectively smooth high spatial frequency hot spots that affect the maximum input power of the compressor, and 60-mm spatial dispersion width is definitely enough to smooth the beam and provide safety for the compressor.

In the output beam with 60-mm spatial dispersion width, the area approximately $(500-60) \times 500$ mm^2 in the middle region owns the same 200 nm full spectral bandwidth, for the rest two 60×500 mm^2 edge parts, they own constantly narrowing spectrum from center to the two edges because of spatial dispersion, which will affect the pulse duration and temporal contrast of the output pulse [21], while, as the amount of spatial dispersion is relatively small compared to the full beam dimension and the intensity of laser beam on two sides is weak, the spatial dispersion impact on the far-field of the output lasers can be almost negligible, which will be discussed behind.

3.3 Near-field beam properties

Assuming that the temporal chirp of the output pulse from the AFGC is well compensated, the near-field spectral- and temporal- spatial couplings caused by the 60-mm spatial dispersion are shown in Fig. 5a and b, respectively, with $Y = 0$.

Figure 5c shows five spectral profiles at positions $X = 0, -200, -220, -240$ and -260 mm in Fig. 5a, only the area from $X = -220$ mm to $X = 220$ mm owns full spectral components, and spectral components decreases with positions drift away from the center beyond the area. This induces the spatiotemporal-coupling as shown in Fig. 5b and d.

Figure 5d shows the temporal profiles at the same positions $X = 0, -200, -220, -240$ and -260 mm in Fig. 5b, the blue dash curve is the temporal profile integration along the X axis, and this curve coincides with the temporal profile at $X = 0$ mm perfectly with a slightly different in the bottom. Pulse durations increase in the areas with X positions lesser than -220 mm and larger than 220 mm.

3.4 Far-field beam properties

Compared with a typical FGC, the AFGC introduces spatial dispersion which may change the far-field properties. A simulation is executed to analyze the impact of the spatial dispersion.

Fig. 5 Spectral- and temporal-spatial properties for the output beam from the AFGC with 60-mm spatial dispersion. **c** Five spectral profiles at positions $X = 0, -200, -220, -240$ and -260 mm in **a**. **d** Five temporal profiles at positions $X = 0, -200, -220, -240$ and -260 mm in **b**, the blue dash curve is the temporal profile integration along the X axis
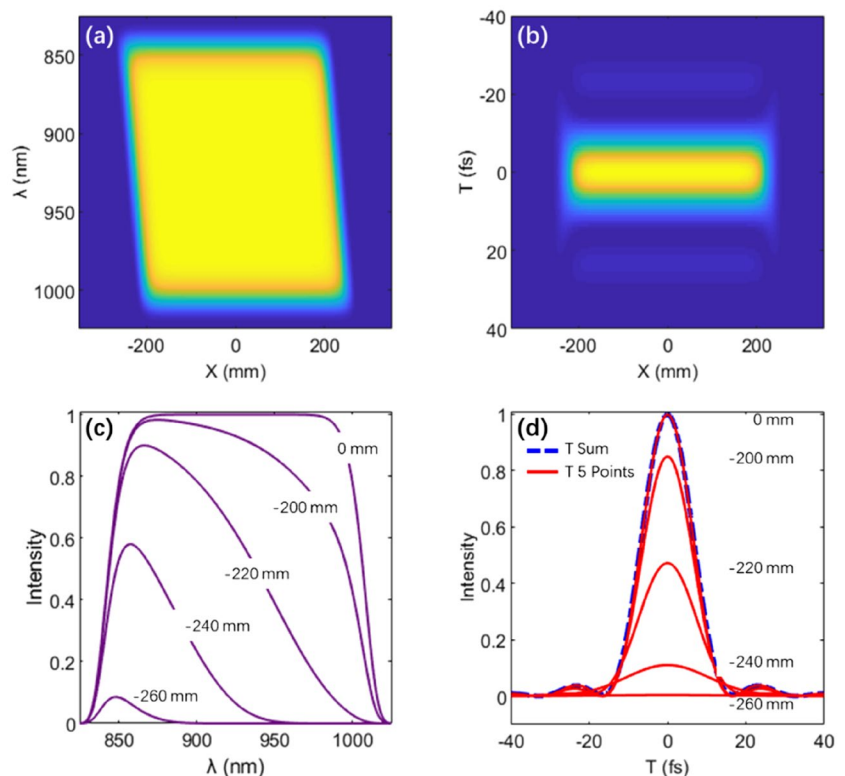
The beam focusing after an AFGC is analog to the spatiotemporal focusing, which has been successfully used in two-photon microscopy and ultrafast micro-machining applications to increase the axial resolution or the optical section function [22, 23].The difference is that the spatial dispersion width is ten times of the incident beam width as for previous application such as micro-machining [23], while in AFGC, less than 0.12 times (60-mm spatial dispersion for 500-mm incident beam width) of spatial dispersion is introduced in the output beam.

A parabolic mirror with 3-m focal length is used to focus the beam. Analytic calculation based on Fresnel diffraction is used to explore the properties around the focal point [22, 27]. For simplicity in the analytic calculation, both the beam and spectrum are assumed to be Gaussian profiles with beam full width about 500 mm and FWHM pulse duration about 14.7 fs. Only the X–Z plane properties are analyzed here as the spatial dispersion is introduced in the horizontal direction. The normalized compensated light field just before the parabolic mirror can be expressed as [22]

$$E_1(x, \Delta\omega) = \exp\left\{ -\frac{\Delta\omega^2}{\Omega^2} \right\}\exp\left\{ -\frac{[x - \alpha\Delta\omega]^2}{W^2} \right\}, \qquad (4)$$

where $\sqrt{2\ln2} \cdot \Omega$ is spectrum width measured at $1/e^2$, $\Delta\omega$ is the frequency difference between spectrum components and the center one, $\sqrt{2\ln2} \cdot W$ is the beam waist measured at $1/e^2$, α is the spatial dispersion coefficient and is defined as the ratio between spatial dispersion width to spectrum FWHM width.

Then the parabolic mirror introduces a phase to the input light field E_1, which can be expressed as

$$E_2(x, \Delta\omega) = E_1(x, \omega)\exp\left(-\mathrm{i}k\frac{x^2}{2f} \right), \qquad (5)$$

where k is the wave vector and f the focal length of the parabolic mirror. Set the position of parabolic mirror to be $z = 0$, then after propagating a distance z of E_2, using the Fresnel diffraction approximation, the light field at z is expressed as

$$E_3(x, z, \Delta\omega) = \frac{W}{2\sqrt{N(1 - \mathrm{i}kW/2f)}}\exp\left[-\frac{(x - P)^2}{4N} + \mathrm{i}\frac{k\alpha\Delta\omega}{f} + Q \right] \qquad (6)$$

where

$$M = \frac{f^2k^2W^4}{4f^2 + k^2W^2} \qquad (6.1)$$

$$N = \frac{M}{k^2W^2} - \mathrm{i}\frac{z - M/f}{2k} \qquad (6.2)$$

$$P = \alpha\Delta\omega(1 - z/f) \qquad (6.3)$$

$$Q = \mathrm{i}\frac{k\alpha^2\Delta\omega^2}{2f^2}(z - f) \qquad (6.4)$$

The intensity at any position is the integral of the contributions of all the $\Delta\omega$ in $|E_3|^2$.

The FWHM pulse duration at z can be expressed as [22].

$$\tau(z) = \frac{1}{\sqrt{Re(1/A)}} \cdot \frac{2\sqrt{2\ln2}}{\Omega} \qquad (7)$$

where k_0 is the wave vector for the center frequency, and $k = k_0$ is approximated for the calculation.

$$A = 1 + \frac{\alpha^2\Omega^2(z - f)^2}{4f^2N} - \mathrm{i}\frac{k_0\alpha^2\Omega^2(z - f)}{2f^2}. \qquad (7.1)$$

Figure 6 shows far-field properties around the focal point. Intensity distributions with no spatial dispersion (Fig. 6a) and 60-mm spatial dispersion (Fig. 6b) in the X–Z planes are almost the same.

The intensity compare in Fig. 6a and b at $x = 0$ is shown in Fig. 6c, for $z - f$ from -100 μm to 100 μm, the two intensity curves coincide well with each other (blue curve for no spatial dispersion and red curve for 60-mm spatial dispersion), the intensity difference becomes stable to be approximately 2.2% relative to the peak intensity at z = f for positions 300 μm away from the focal plane as shown as the right Y axis purple curve.

In Fig. 6d, the beam profiles of Fig. 6a, b at positions z = f and at 400 μm before the focal point are compared, beam profiles coincide with each other perfectly at z = f, and only slight differences exist for the beam width and intensity at 400 μm before the focal point, the intensity difference is approximately 2.2% relative to the peak intensity at z = f, and FWHM beam width increases approximately 2.7% (from 18.8 μm when with no spatial dispersion to 19.3 μm when with 60 mm spatial dispersion). Figure 6e shows the FWHM pulse duration variation because of the spatial dispersion from Eq. (7), just 0.48% duration (0.07 fs) increases at the positions 400 μm before or behind the focal point.

It can be concluded that the 60-mm spatial dispersion in the simulation condition, which is definitely enough to smooth the beam and provide safety for the compressor, barely brings impact to the intensity profiles around the focal point.

From Fig. 6, we can see that the beam width and pulse duration for beams with or without the 60-mm spatial dispersion for the 500-mm full width input beam are all the same in the focal plane. While in applications, targets can hardly be located in the focal plane, we explored the spatial and temporal properties at the positions 100 μm before the focal points for different focal lengths $f = 1, 2$, and 3 m. The input beams own different beam widths from 100 to
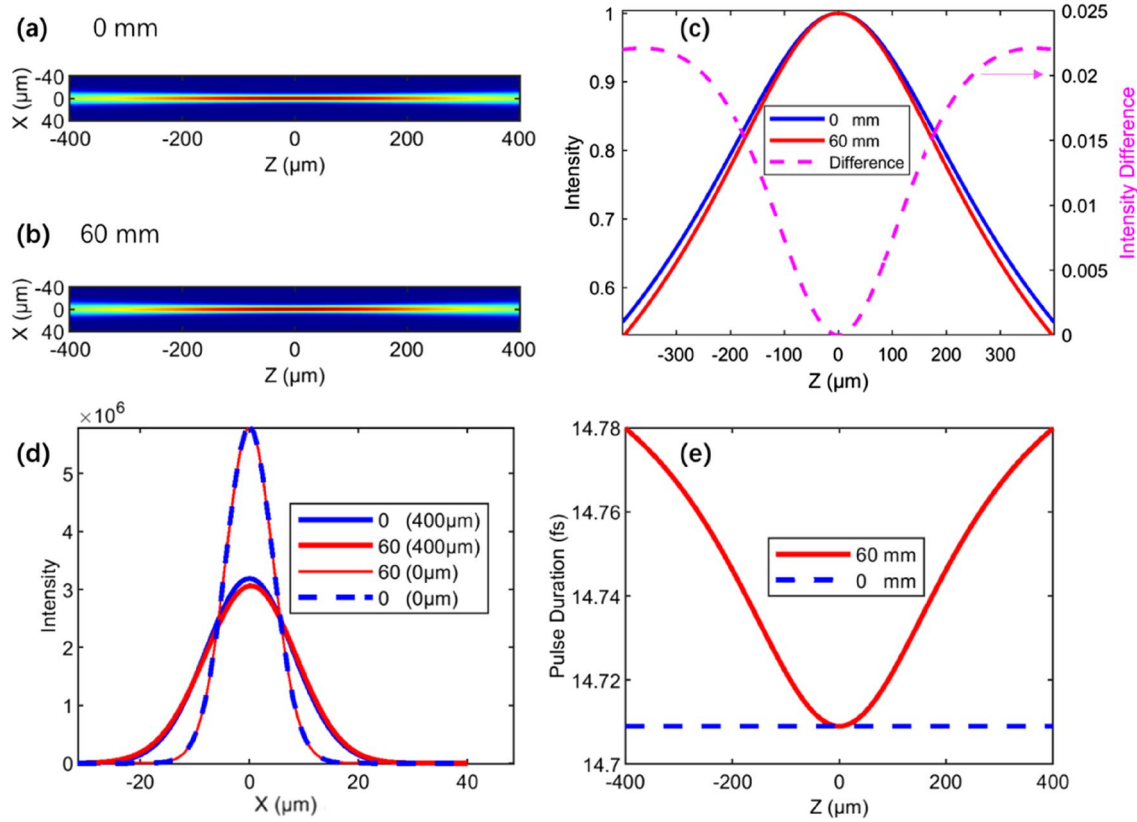
Fig. 6 Intensity distributions in X–Z planes for beams without **a** and with 60 mm spatial dispersion **b**. **c** Intensity profiles compare in **a** and **b** at x = 0. **d** Beam profiles compare of **a**, **b** at positions z = f and at 400 μm before the focal point. **e** FWHM pulse duration variation for pulse with 60 mm or without spatial dispersion

1500 mm while own the same 60-mm spatial dispersion and the same spectrum components corresponding to approximately 14.71 fs FTL FWHM pulse duration.

In Fig. 7, the purple curves are FWHM pulse duration variations and the rest are the far-field focused FWHM beam width variations. Without spatial dispersion, the pulse durations keep the same as shown of the purple dot line, and the beam widths are shown as the blue solid lines. With 60-mm spatial dispersion, the rest three purple curves show the pulse duration variations, and the three red dash curves show the beam width variations. The beam width is inverse proportional to the input beam widths in the focal plane. While out of the focal plane, as shown in Fig. 7, the beam widths at positions 100 μm before the focal points do not evolve monotone, and extremums occur at input beam widths 250 mm, 550 mm and 800 mm for f = 1, 2, and 3 m, respectively.

The compare of far-field beam widths for beams with or without 60-mm spatial dispersion shows that focus with shorter focal length causes bigger differences around the extremums, while with input beam widths become farther and farther away from the extremums, the far-field beam widths for beams with or without spatial dispersion
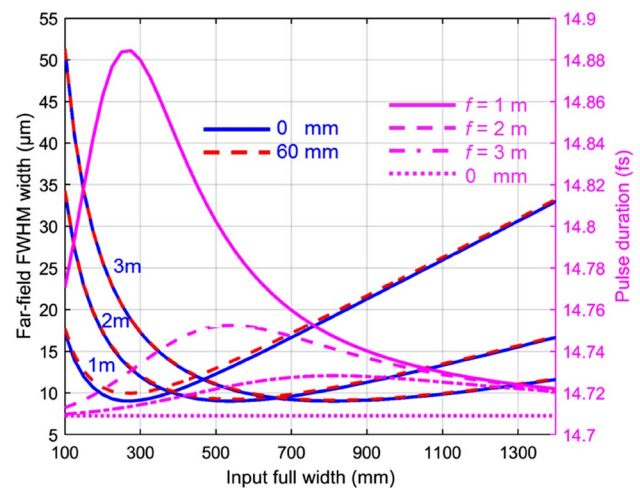

Fig. 7 Far-field beam FWHM width and pulse duration variations relative to input beam full widths. The input beams own the same spectrum components and the spatial dispersion width is 60 mm

coincide better and better. The increase of the far-field beam width because of the spatial dispersion decreases the spectrum components, and brings pulse duration

increase. For $f = 1$ m and at the extremum input beam width 250 mm, the far-field beam width increases from about 9.06 μm to 10.01 μm, which makes the pules duration to increase from 14.71 fs to the largest 14.89 fs (about 1.2%, 0.18 fs).

In the focal plane, as the light field is the Fraunhofer pattern of the light field before the parabolic mirror with $z = f$, incident light field can be easily obtained [28]. The properties in the focal plane with parameters listed in

Table 1 are simulated with the approximation of $k = k_0$ and is shown as Fig. 8.

Figure 8a–c show spatiotemporal properties at the focal plane when there is spatial dispersion ($d0 = 60$ mm), and Fig. 8d–f when there is no spatial dispersion ($d0 = 0$ mm). It can be found that the introduced spatial dispersion along the horizontal direction induces a slightly pulse front tilt in the *Vertical vs. Time* plane (Fig. 8b). In the time domain, the $d0 = 60$ mm spatial dispersion slightly broaden the

Table 1 Simulation parameters

Beam size incident to the AFGC (full width)	500×500 mm^2
Beam intensity profile	10th order super-Gaussian
Center wavelength/full spectral bandwidth	925 nm/200 nm
Spectrum profile	6th order super-Gaussian
Chirped pulse duration	~4 ns
FTL pulse duration	~14.7 fs
Groove density of gratings	1400 lines/mm
Incident angle of the AFGC	61°
Total perpendicular length of the two grating pairs ($L1 + L2$)	~2480 mm
FWHM diameters of hot spots of Gaussian shape	0.25, 0.5, 1, 2, 4, 6, 8 (mm)

Fig. 8 Spatiotemporal properties at the focal plane with and without spatial dispersion on the laser beam. Spatiotemporal properties, and the integrated spatial profiles at the focal plane in the case of **a**–**c** with $d0 = 60$ mm spatial dispersion along the horizontal direction, and **d**–**f** with no spatial dispersion ($d0 = 0$ mm), respectively. **g**–**h** Temporal profiles when (**g**) $X = 0$ mm in Horizontal-T plane, **h** $Y = 0$ mm in vertical-T plane, and **i** the integrated temporal profiles in log scale at the focal plane. Red solid curves: without spatial dispersion; blue dash and solid curves: with $d0 = 60$ mm spatial dispersion along the horizontal direction
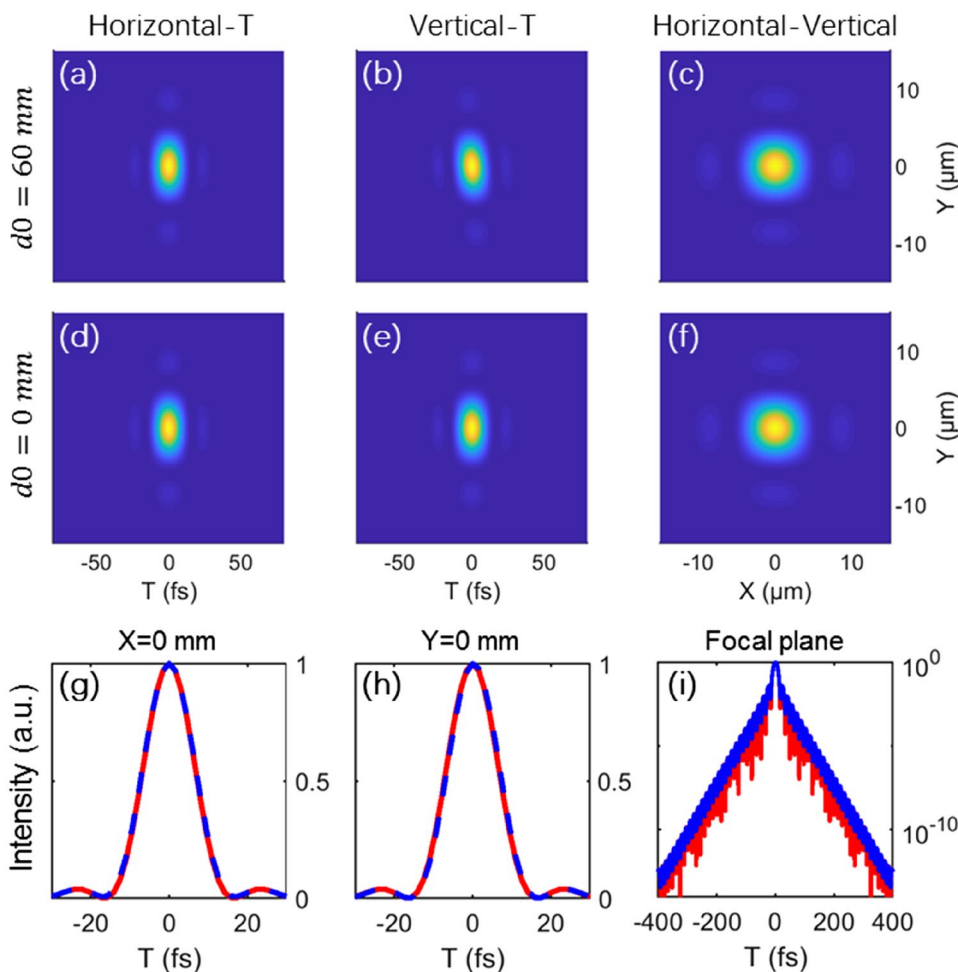
pulse duration in the *Horizontal vs. Time* plane as shown in Fig. 8g, and for the total pulse duration in log scale at the focal plane as shown in Fig. 8i, the influence can be almost negligible. The red solid curves in Fig. 8g–i show the approximately 14.7 fs FTL pulse durations without spatial dispersion and the blue dash curves the pulse durations with spatial dispersion, they almost coincide. In the spatial domain, the focal diameters are almost the same for both beams, as shown in Fig. 8c and f.

As a result, both the focal diameter and the pulse duration at the focal plane are barely affected by the 60-mm width spatial dispersion.

3.5 AFGC compression for a FTL 47 fs pulse centered at 800 nm

A pulse centered at 800 nm with 63 nm full bandwidth and spectrum profile Gaussian shape output from a Ti: sapphire CPA system is used to verify the AFGC method experimentally. The amplified beam with diameter of approximately 12 mm is guided to a four-grating compressor. The incident angle is 54°, and the groove density of the gratings is 1480 lines/mm. In the condition the compressor is a typical FGC with symmetric structure, perpendicular distances of its two grating pairs $L1$ and $L2$ are both 297 mm to compensate the pulse chirp. A distance difference of 100 mm ($L2-L1$) makes
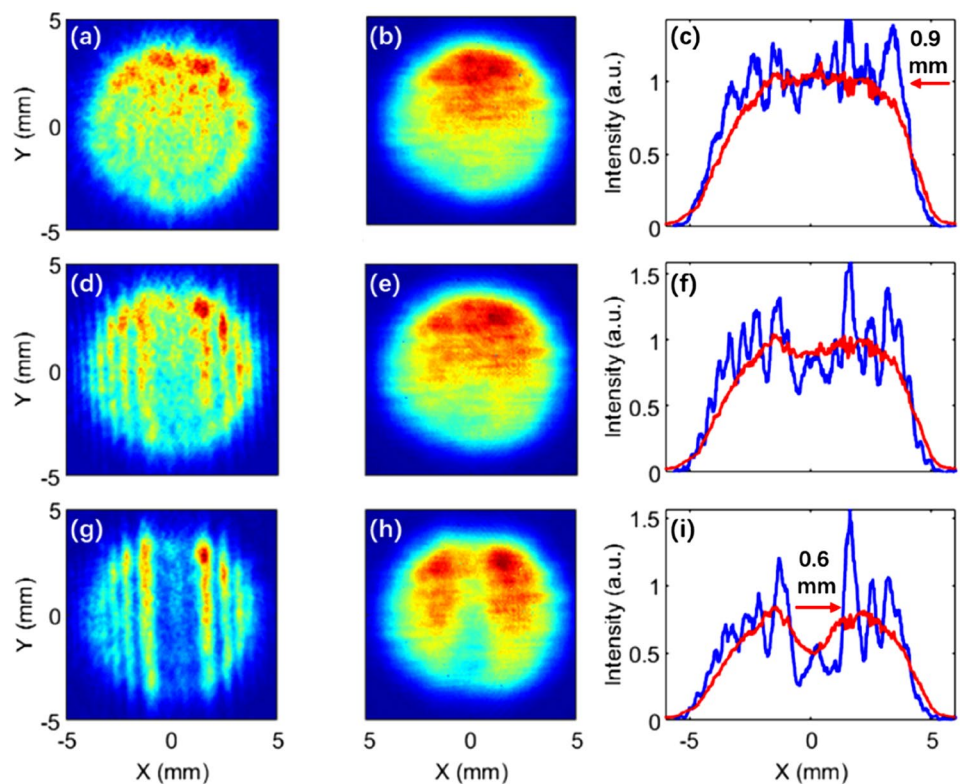
the compressor an AFGC structure, which introduces an approximately 6.9-mm spatial dispersion to the output beam.

Output beams from the compressor are converged by a 500-mm focal length lens to a CCD for beam profile measurement. In Fig. 9, the first row shows the beams measured when the compressor is a typical FGC, the second row shows the beams measured when the compressor is an AFGC, and the last row compares the intensity modulations at $Y=0$ for beams in the same line (blue for FGC and red for AFGC). A hair and an about 0.8-mm-wide paper riband are added at the middle of the input beams to introduce higher modulations as shown in the second and third lines in Fig. 9, respectively.

It can be concluded from Fig. 9 that, both the high modulations exist inherently in the input beam and the higher modulations introduced by the hair can be smoothed effectively by the induced 6.9-mm-wide spatial dispersion through AFGC. Hot spots as wide as 0.9 mm can be smoothed out. The sunk parts at the middle of the profile curves in Fig. 9i and f show that the paper riband cause energy losses and wide gap which can also be smoothed.

For the same AFGC, the induced spatial dispersion widths are different for different incident angles and spectrum widths according to Eq. (3). The broader the bandwidth, the larger the spatial dispersion can be introduced. While for the same spatial dispersion, the amounts of LSIM decrease different for different shapes of spectrum profiles. For ultrashort PW lasers with bandwidths to be

Fig. 9 Measured beams when the compressor is a typical FGC (**a**, **d**, **g**), and when the compressor is an AFGC (**b**, **e**, **h**). **c**, **f**, **i** compare the intensity modulations at $Y=0$ for beams in the same line (blue for FGC and red for AFGC). A hair and an about 0.8-mm-wide paper riband are added at the middle of the input beams to introduce higher modulations in the second and third lines, respectively. The 0.9 mm in **c** and 0.6 mm in **i** are the hot spots widths pointed by the arrows

approximately 200 nm and spectrum of high order super-Gaussian profile, the AFGC structure of the compressor can introduce spatial dispersion and smooth the output beam easily.

The incident pulse has an FTL duration of 47 fs with its spectrum profile shown as Fig. 10a. The far-field temporal properties are measured by a home-made SHG-FROG device. Similar properties of temporal and phase profiles are measured with approximately 57 fs FWHM duration for both

the FGC and AFGC structures as shown in Fig. 10b and f in linear and log scale, respectively. For the main pulses, they coincide well with each other. The two beams are focused by a 500-mm focal length lens for focal spots measurement. The measured focal spots for both the FGC and AFGC structures are shown in Fig. 10c and d, respectively, with about 96 μm full width diameters shown in Fig. 10e. The intensity profiles at $X=0$ (AFGC-x and FGC-x in Fig. 10e) coincide well, while a slightly broadening exists for the AFGC structure
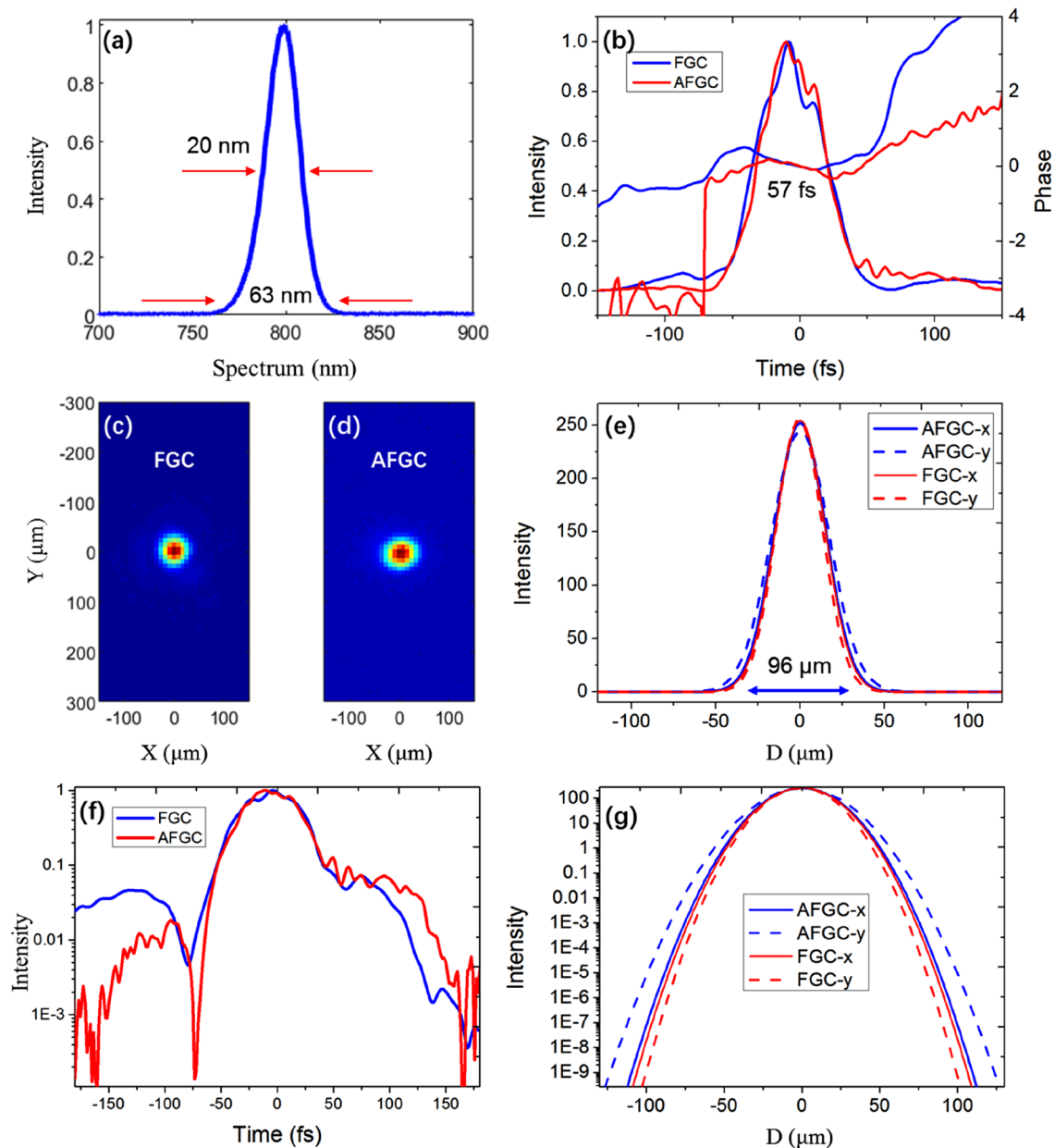

Fig. 10 **a** Spectrum profile of the incident beam. **b** Temporal properties of beams output from the FGC and AFGC compressors. **c** and **d** Focal spots for beams output from the FGC and AFGC compressors, respectively. **e** Beam profiles at $X=0$ (solid curves) and $Y=0$ (dashed curves) of the focal spots shown in **c** and **d**. **f** Temporal profiles in log scale. **g** Beam profiles in log scale. Curves in **e** and **f** are Gaussian smoothed from the beam profiles at $X=0$ and $Y=0$ in **c** and **d**

compared with the FGC structure at $Y = 0$ (AFGC-y and FGC-y in Fig. 10e). Figure 10g shows the log scale intensity profiles. It shows that the beam profile difference between the two situations along the horizontal direction is obvious. This may be caused by the non-ideal focus, what is more, the 6.9-mm spatial dispersion to the 12-mm input beam is large enough and may cause an obvious intensity plane tilt (IPT) and increase the beam width [23].

The experimental result shows that the AFGC can smooth the laser beam effectively, but barely brings impact to pulse properties in the focal plane.

3.6 AFGC-based two-step MPC for tens PW lasers

Figure 11 shows a typical optical configuration of the AFGC-based two-step MPC, where there is no prism-pair-based pre-compressor, the typical FGC with symmetric configuration is replaced by an AFGC, and the post-compressor is the same, just a parabolic reflective mirror PM [17]. Firstly, the input beam is pulse front compensated by a deformable mirror (DM) and expanded by a beam expander (BE). Then, the expanded beam is led into the first compression stage, the AFGC, where spectral and spatial dispersion are introduced for the chirped pulse compression and LSIM decreasing of the output beam, respectively. Finally, a parabolic reflective mirror PM is used for the post-compressor to automatically compensate the introduced spatial dispersion at the focal plane [17, 22, 23].

In the AFGC, the laser-induced damage threshold on the first and final grating are different owing to different pulse duration on the two gratings. Experimental data have been
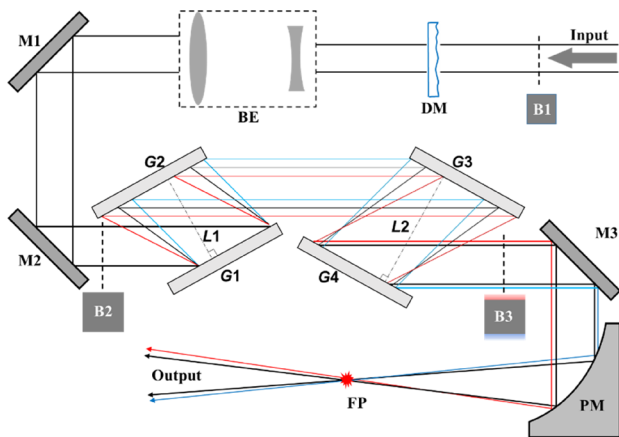
concluded that the laser-induced damage threshold ratio between the first and the final gratings is approximately 2.67:1 owing to nanosecond and femtosecond pulse duration on them, respectively [10, 17]. In the condition that the LSIM of the laser beam is decreased from approximately 2.0 on the first grating to 1.1 on the final grating with 60-mm spatial dispersion, the maximum fluence the first grating can bear still keeps the same that 0.5 times of its laser-induced damage threshold, while the final grating can bear increases from approximately 0.5 times to 0.9 times of its laser-induced damage threshold. Considering the fluence ratio between the first and final grating is approximately 1.37:1 supposing the diffraction efficiency is 90% on each grating, in the condition that the final grating bears the maximum fluence with LSIM is 1.1, the fluence on the first grating is still under 0.5 times of its laser-induced damage threshold, and the AFGC can still operate safe and sound. Obviously, the AFGC-based two-step MPC is easier and simpler than that of the typical three-step MPC.

As an example, with the optical parameters in the above simulation, as the femtosecond laser-induced damage threshold fluence is approximately 229 mJ/cm^2 for the typical gold-coated diffraction grating [17], and the input beam size is 500×500 mm^2, the total output power of the AFGC can then be approximately 500×500 mm$^2 \times 229$ mJ/cm^2/cos61°/1.1/15 fs$\approx$71 PW, where the LSIM of the output beam is approximately 1.1 with spatial dispersion width $d0 = 60$ mm, the pulse duration is approximately 15 fs and input angle of grating is 61°. It means 50 PW can be obtained safely. With gratings of size as large as 700×1450 mm^2 that are available at present which can almost support the input beam size of approximately 550×700 mm^2 with almost no spectral shearing, the power can be increased to approximately 550×700 mm$^2 \times 229$ mJ/cm^2/cos61°/1.1/15 fs$\approx$110 PW theoretically.

4 Discussion and conclusion

Laser-induced damage is a serious limitation in PW lasers as the strong fluence may damage optical components with limited sizes and damage thresholds, where gratings in compressors have been the shortest stave of PW lasers up to now. This is because manufacturing a high quality meter-sized grating remains particularly challenging [9, 10]. Methods such as the tiled grating and the CBC were proposed that use size limited gratings in a tiled way or a multi beams compression way to achieve high power laser output. Recently, typical MPC method with three steps was proposed to increase the maximum input/output pulse energy by reducing LSIM of laser beams.

Here, using the AFGC in the MPC, the three-step MPC is simplified into two steps which can be achieved very easily

Fig. 11 Typical optical configuration of the AFGC-based two-step MPC. DM, deformable mirrors for pulse front compensating. BE, beam expander. M1-3, reflective mirrors. G1-4, diffraction gratings. $L1 < L2$, PM, parabolic reflective mirror. FP, focal point. B1, B2 and B3 are the schematic beam profiles at the positions of the three dash lines, the dark gray areas contain full spectra, and the red and blue areas in B3 contain partial longer and shorter spectra, respectively

by simply change the two grating pair distances a little bit in traditional FGC with symmetric configuration. As a result, this method can be extended very conveniently to all current PW laser facilities with FGC to protect the last grating and improve their maximum output pulse energy. The method is based on spatiotemporal property modification to decrease LSIM of the laser beam directly in AFGC compressor. According to the simulation, it is an effective way to decrease the LSIM from approximately 2.0 to 1.1 if introduce sufficient spatial dispersion of 60 mm, and the spatial dispersion barely brings impact to pulse properties around the focal point. According to a previous work, even a picosecond PW laser, the OMEGA-EP facility, can smooth the tiled grating gap induced LSIM using AFGC configuration-induced approximately 2-mm width spatial dispersion [20].

In conclusion, an AFGC-based two-step MPC method is proposed and studied for femtosecond PW lasers compression which can improve the operating safety and increase the maximum bearable output pulse energy of femtosecond PW lasers. More than 100 PW output power can be achieved with single beam in theory by using this method and current available gratings. Together with post compression with thin films or thin glass plates [24–26] after the AFGC with smoothed laser beam, higher peak power is expected to be obtained in the future.

Declarations

Conflict of interest The authors declare no conflicts of interest.

References

1. D. Strickland, G. Mourou, Compression of amplified chirped optical pulses. Opt. Commun. **56**, 219–221 (1985)
2. A. Dubietis, G. Jonusauskas, A. Piskarskas, Powerful femtosecond pulse generation by chirped and stretched pulse parametric amplification in bbo crystal. Opt. Commun. **88**, 437–440 (1992)
3. N. Danson, C. Haefner, J. Bromage, T. Butcher, J.-C. F. Chanteloup, E. A. Chowdhury, A. Galvanauskas, L. A. Gizzi, J. Hein, D. I. Hillier, N. W. Hopps, Y. Kato, E. A. Khazanov, R. Kodama, G. Korn, R. Li, Y. Li, J. Limpert, J. Ma, C. H. Nam, D. Neely, D. Papadopoulos, R. R. Penman, L. Qian, J. J. Rocca, A. A. Shaykin, C. W. Siders, C. Spindloe, S. Szatmari, R. M. G. M. Trines, J. Zhu, P. Zhu, and J. D. Zuegel, "Petawatt and exawatt class lasers worldwide," High Power Laser Sci. Eng. **7**, e54, 1–54 (2019)
4. F. Lureau, G. Matras, O. Chalus, C. Derycke, T. Morbieu, C. Radier, O. Casagrande, S. Laux, S. Ricaud, G. Rey, A. Pellegrina, C. Richard, L. Boudjemaa, C. Simon-Boisson, A. Baleanu, R. Banici, A. Gradinariu, C. Caldararu, B. D. Boisdeffre, P. Ghenuche, A. Naziru, G. Kolliopoulos, L. Neagu, R. Dabu, I. Dancus, and D. Ursescu, "High-energy hybrid femtosecond laser system demonstrating 2 x 10 PW capability," High Power Laser Sci. Eng. **8**, e43, 1–15 (2020)
5. Z. Gan, L. Yu, C. Wang, Y. Liu, Y. Xu, W. Li, S. Li, L. Yu, X. Wang, X. Liu, J. Chen, Y. Peng, L. Xu, B. Yao, X. Zhang, L. Chen, Y. Tang, X. Wang, D. Yin, X. Liang, Y. Leng, R. Li, and Z. Xu (2021) "The Shanghai Superintense Ultrafast Laser Facility (SULF) Project," In *Progress in Ultrafast Intense Laser Science Xvi*, K. Yamanouchi, K. Midorikawa, and L. Roso, (eds), pp. 199–217 (Springer, Switzerland, 2021)
6. G.A. Mourou, T. Tajima, S.V. Bulanov, Optics in the relativistic regime. Rev. Mod. Phys. **78**, 309–371 (2006)
7. E. Cartlidge, The light fantastic. Science **359**, 382–385 (2018)
8. B. Shen, Z. Bu, J. Xu, T. Xu, L. Ji, R. Li, Z. Xu, Exploring vacuum birefringence based on a 100 PW laser and an x-ray free electron laser beam. Plasma Phys. Controlled Fusion **60**(4), 044002 (1–11) (2018)
9. J. Liu, X. Shen, Z. Si, C. Wang, C. Zhao, X. Liang, Y. Leng, R. Li, In-house beam-splitting pulse compressor for high-energy petawatt lasers. Opt. Express **28**, 22978–22991 (2020)
10. N. Bonod, J. Neauport, Diffraction gratings: from principles to applications in high-intensity lasers. Adv. Opt. Photon. **8**, 156–199 (2016)
11. J. Qiao, A. Kalb, T. Nguyen, J. Bunkenburg, D. Canning, J.H. Kelly, Demonstration of large-aperture tiled-grating compressors for high-energy, petawatt-class, chirped-pulse amplification systems. Opt. Lett. **33**, 1684–1686 (2008)
12. N. Blanchot, G. Marre, J. Neauport, E. Sibe, C. Rouyer, S. Montant, A. Cotel, C. Le Blanc, C. Sauteret, Synthetic aperture compression scheme for a multipetawatt high-energy laser. Appl. Opt. **45**, 6013–6021 (2006)
13. V.E. Leshchenko, V.A. Vasiliev, N.L. Kvashnin, E.V. Pestryakov, Coherent combining of relativistic-intensity femtosecond laser pulses. Appl. Phys. B-Lasers Opt. **118**, 511–516 (2015)
14. C. Peng, X. Liang, R. Liu, W. Li, R. Li, High-precision active synchronization control of high-power, tiled-aperture coherent beam combining. Opt. Lett. **42**, 3960–3963 (2017)
15. N. Blanchot, G. Behar, J.C. Chapuis, C. Chappuis, S. Chardavoine, J.F. Charrier, H. Coic, C. Damiens-Dupont, J. Duthu, P. Garcia, J.P. Goossens, F. Granet, C. Grosset-Grange, P. Guerin, B. Hebrard, L. Hilsz, L. Lamaignere, T. Lacombe, E. Lavastre, T. Longhi, J. Luce, F. Macias, M. Mangeant, E. Mazataud, B. Minou, T. Morgaint, S. Noailles, J. Neauport, P. Patelli, E. Perrot-Minnot, C. Present, B. Remy, C. Rouyer, N. Santacreu, M. Sozet, D. Valla, F. Laniesse, 1.15 PW-850 J compressed beam demonstration using the PETAL facility. Opt. Express **25**, 16957–16970 (2017)
16. D. Wang, Y. Leng, Simulating a four-channel coherent beam combination system for femtosecond multi-petawatt lasers. Opt. Express **27**, 36137–36153 (2019)
17. J. Liu, X. Shen, S. Du, R. Li, Multistep pulse compressor for 10s to 100s PW lasers. Opt. Express **29**(11), 17140–17158 (2021)
18. E.B. Treacy, Optical pulse compression with diffraction gratings. IEEE J. Quantum Electron **5**, 454 (1969)
19. P. Poole, S. Trendafilov, G. Shvets, D. Smith, E. Chowdhury, Femtosecond laser damage threshold of pulse compression gratings for petawatt scale laser systems. Opt. Express **21**, 26341–26351 (2013)
20. H. Huang, T. Kessler, Tiled-grating compressor with uncompensated dispersion for near-field-intensity smoothing. Opt. Lett. **32**, 1854–1856 (2007)
21. M. Trentelman, I.N. Ross, C.N. Danson, Finite size compression gratings in a large aperture chirped pulse amplification laser system. Appl. Opt. **36**, 8567–8573 (1997)
22. G.H. Zhu, J. van Howe, M. Durst, W. Zipfel, C. Xu, Simultaneous spatial and temporal focusing of femtosecond pulses. Opt. Express **13**, 2153–2159 (2005)

23. F. He, B. Zeng, W. Chu, J. Ni, K. Sugioka, Y. Cheng, C.G. Durfee, Characterization and control of peak intensity distribution at the focus of a spatiotemporally focused femtosecond laser beam. Opt. Express **22**, 9734–9748 (2014)

24. J. Liu, X.W. Chen, J.S. Liu, Y. Zhu, Y.X. Leng, J. Dai, R.X. Li, Z.Z. Xu, Spectrum reshaping and pulse self-compression in normally dispersive media with negatively chirped femtosecond pulses. Opt. Express **14**, 979–987 (2006)

25. V. Ginzburg, I. Yakovlev, A. Zuev, A. Korobeynikova, A. Kochetkov, A. Kuzmin, S. Mironov, A. Shaykin, I. Shaikin, E. Khazanov, G. Mourou, Fivefold compression of 250-TW laser pulses. Phys. Rev. A **101**(1), 013829 (1–6) (2020)

26. Z. Li, Y. Kato, J. Kawanaka, Simulating an ultra-broadband concept for Exawatt-class lasers. Sci. Rep. **11**, 151 (1–16) (2021)

27. F. He, Y. Cheng, J. Lin, J. Ni, Z. Xu, K. Sugioka, K. Midorikawa, Independent control of aspect ratios in the axial and lateral cross sections of a focal spot for three-dimensional femtosecond laser micromachining. New J Phys **13**(8), 083014 (1-13) (2011)

28. D. Voelz, *Computational Fourier Optics A MATLAB Tutorial, Chap 6* (SPIE, Washngton, 2011)